AFRL-RD-PS
TP-2010-1018

IMPROVING IMAGING THROUGH TURBULENCE VIA APERTURE PARTITIONING: POSTPRINT

Brandoch Calef

Boeing LTS
535 Lipoa Parkway Suite 200
Kihei HI 96753

9 February 2010

Technical Paper

AIR FORCE RESEARCH LABORATORY
Directed Energy Directorate
3550 Aberdeen Ave SE
AIR FORCE MATERIEL COMMAND
KIRTLAND AIR FORCE BASE, NM 87117-5776

REPORT DOCUMENTATION PAGE

Form Approved
OMB No. 0704-0188

1. REPORT DATE *(DD-MM-YYYY)*	2. REPORT TYPE	3. DATES COVERED *(From - To)*
09-02-2010	Technical Paper	April 1, 2006- February 9, 2010

4. TITLE AND SUBTITLE

Improving Imaging through Turbulence Via Aperture Partitioning

5a. CONTRACT NUMBER
FA9451-05-C-0257 M024AIR DF297701

5b. GRANT NUMBER

5c. PROGRAM ELEMENT NUMBER

6. AUTHOR(S)

Brandoch Calek

5d. PROJECT NUMBER

5e. TASK NUMBER

5f. WORK UNIT NUMBER

7. PERFORMING ORGANIZATION NAME(S) AND ADDRESS(ES)

Boeing LTS
535 Lipoa Parkway, Suite 200
Kihei, HI 96753

8. PERFORMING ORGANIZATION REPORT NUMBER

9. SPONSORING / MONITORING AGENCY NAME(S) AND ADDRESS(ES)

Air Force Research Laboratory
3550 Aberdeen Ave SE
Kirtland AFB NM 87117-5776

10. SPONSOR/MONITOR'S ACRONYM(S)
AFRL/RDSM

11. SPONSOR/MONITOR'S REPORT NUMBER(S)
AFRL-RD-PS-TP-2010-1018

12. DISTRIBUTION / AVAILABILITY STATEMENT

Approved for public release

13. SUPPLEMENTARY NOTES
Accepted for publication at the SPIE DSS Conference; Orlando, Florida; April 7, 2010. 377ABW-2010-0176; Feb 9, 2010. "GOVERNMENT PURPOSE RIGHTS"

14. ABSTRACT
Speckle imaging techniques make it possible to do high-resolution imaging through the turbulent atmosphere by collecting and processing a large number of short-exposure frames, each of which effectively freezes the atmosphere. In severe seeing condition, when the characteristic scale of atmospheric fluctuations is much smaller than the diameter of the telescope, the reconstructed image is dominated by "turbulence noise" caused by redundant baselines in the pupil. I describe a generalization of aperture masking interferometery that dramatically improves imaging performance in this regime. The approach is to partition the aperture into annuli, form the bispectra of the focal plane images formed from each annulus, and recombine them into a synthesized bispectrum form which the object may be retrieved. This may be implemented using multiple cameras and special mirrors, or with a single camera and a suitable pupil phase mask. I report results from simulations as well as experimental results using telescopes at the Air Force Research Lab's Maui Space Surveillance Site.

15. SUBJECT TERMS

16. SECURITY CLASSIFICATION OF:			17. LIMITATION OF ABSTRACT	18. NUMBER OF PAGES	19a. NAME OF RESPONSIBLE PERSON
					Casey Pellizzari
a. REPORT	b. ABSTRACT	c. THIS PAGE			19b. TELEPHONE NUMBER *(include area code)*
Unclassified	Unclassified	Unclassified	SAR	14	808-874-1538

Standard Form 298 (Rev. 8-98)
Prescribed by ANSI Std. 239.18

This page is intentionally left blank.

Improving imaging through turbulence via aperture partitioning

Brandoch Calef
Boeing LTS Maui, 535 Lipoa Parkway Suite 200, Kihei HI 96753

ABSTRACT

Speckle imaging techniques make it possible to do high-resolution imaging through the turbulent atmosphere by collecting and processing a large number of short-exposure frames, each of which effectively freezes the atmosphere. In severe seeing conditions, when the characteristic scale of atmospheric fluctuations is much smaller than the diameter of the telescope, the reconstructed image is dominated by "turbulence noise" caused by redundant baselines in the pupil. I describe a generalization of aperture masking interferometry that dramatically improves imaging performance in this regime. The approach is to partition the aperture into annuli, form the bispectra of the focal plane images formed from each annulus, and recombine them into a synthesized bispectrum from which the object may be retrieved. This may be implemented using multiple cameras and special mirrors, or with a single camera and a suitable pupil phase mask. I report results from simulations as well as experimental results using telescopes at the Air Force Research Lab's Maui Space Surveillance Site.

1. INTRODUCTION

When images are collected through the atmosphere, they are distorted due to refractive index fluctuations along the turbulent path [1]. The object may be recovered by the bispectrum technique, which exploits phase closure and atmospheric statistics to provide an estimate of the object's Fourier phase. As the ratio D/r_0 of the telescope aperture diameter to the atmospheric seeing cell size increases, the optical transfer function (OTF) is attenuated and the number of redundant baselines in the pupil increases, driving down the SNR of the bispectrum estimate.

The usual way of overcoming the latter degradation (which is sometimes called "baseline redundancy noise") is to collect short exposure images for many atmospheric decorrelation times. Averaging together their bispectra increases the SNR of the object bispectrum estimate in proportion to the square root of the number of independent atmospheric realizations. However, this approach is not always practical. For example, suppose that the subject of observation is a satellite passing overhead. Every few seconds, its orientation relative to the observer changes by an amount that is significant at the resolution of the telescope. This puts a limit on the time interval of frames that can be safely co-processed.

Another way of defeating redundancy noise is to mask the aperture, either with a pattern of holes whose diameters are on the order of r_0 (a non-redundant mask) or with a thin annulus at the outer edge of the pupil (a partially redundant mask). This approach is called aperture masking interferometry [2]. It eliminates or greatly reduces baseline redundancy noise at the expense of a much lower signal. This means that it can only be applied when the object is bright or when frames can be collected over a long period of time to accumulate signal.

In the following pages, I describe a way to extend this technique by partitioning the pupil and measuring the speckle patterns associated with each section. In this way, the redundancy noise is reduced while still making use of all light incident on the aperture. The natural partition is a set of concentric annuli, with the outermost ring providing information up to the diffraction limit of the telescope.

2. BISPECTRUM RECONSTRUCTION

2.1 Review of bispectrum technique

The object will be reconstructed from speckle images using the bispectrum, which we now review. Let $i(x)$ be a speckle image (focal-plane intensity pattern) formed by convolving an object $o(x)$ with an atmospheric point-spread function (PSF) $h(x)$. In Fourier space, this is written $I(u) = O(u)H(u)$. The bispectrum of $i(x)$ is defined by $B_I(u,v) = I(u)I(v)I^*(u+v)$, where u and v are both spatial frequencies. The bispectra of the object, PSF, and speckle image are therefore related by $B_I(u,v) = B_O(u,v)B_H(u,v)$. It can be shown that the expected bispectrum $\langle B_H(u,v)\rangle$ of the atmospheric PSF has zero phase (this will be discussed below), so the ensemble average speckle bispectrum has the same phase as the object bispectrum. From the bispectrum phase, the object's Fourier phase may be recovered up to an overall linear phase, which corresponds to a translation of the reconstructed image.

To implement this approach, a sequence of speckle images is collected and an estimate formed of the bispectrum of each one. In the presence of noise, an unbiased estimator of the bispectrum is given by

$$\hat{B}_I(u,v) = I(u)I(v)I^*(u+v) - |I(u)|^2 - |I(v)|^2 - |I(u+v)|^2 + 2K + 3n_{\text{pix}}\sigma^2, \tag{1}$$

where K is the number of photoelectrons, n_{pix} is the number of pixels, and σ^2 is the read noise variance in each pixel in photoelectrons. The bispectra of the individual frames are averaged together to form an ensemble estimate.

To see how the object may be recovered, consider the relationship between its Fourier phase and the bispectrum, given by $\arg B_O(u,v) = \arg O(u) + \arg O(v) - \arg O(u+v)$. Thus if the phase is known at u and v, it may be recovered at $u+v$ by

$$\arg O(u+v) = \arg O(u) + \arg O(v) - \arg B_O(u,v). \tag{2}$$

To get this process started, observe that the dc term is always real, so $\arg O(0) = 0$. The choice of the first off-dc Fourier components governs the translation of the reconstructed image, which is arbitrary. From this point, repeatedly applying Eqn. 2 yields the entire phase map.

Having recovered the object's Fourier phase, one needs only the amplitude $|O(u)|$ to obtain a complete reconstruction. This may be achieved by making observations of a star under similar atmospheric conditions and using these to estimate the speckle transfer function $\langle |H|^2 \rangle$. Then

$$|O| = \left(\langle |I|^2 \rangle / \langle |H|^2 \rangle \right)^{1/2}. \tag{3}$$

2.2 Bispectrum estimation with a partitioned aperture

The effectiveness of the bispectrum technique hinges on the convergence of the bispectra of observed atmospheric PSFs to the purely real ensemble average. Taking the pupil amplitude to be unity and recalling that $H(u)$ is the autocorrelation of the pupil complex amplitude, the bispectrum of a wavefront with phase ϕ in the pupil is

$$\begin{aligned} B_H(u,v) = &\int_{P(0)\cap P(u)} \exp(i(\phi(w) - \phi(w+u)))\,dw \\ &\times \int_{P(0)\cap P(v)} \exp(i(\phi(w) - \phi(w+v)))\,dw \\ &\times \int_{P(0)\cap P(u+v)} \exp(i(\phi(w+u+w) - \phi(w)))\,dw, \end{aligned} \tag{4}$$

where $P(z)$ is the set of points in the pupil shifted by z. As the number of atmospheric cells in the pupil increases (due to increasing D or decreasing r_0), the integral product yields a larger number of uncancelled phasor contributions to $B_H(u,v)$. This is the source of baseline redundancy noise.

Suppose that instead of a single full pupil, speckle images are collected simultaneously from several subregions of the aperture. If the aperture partition is constructed in such a way that the number of points in each region having a given vector separation is small, then the redundancy noise in the bispectrum estimate will be reduced.

Let $h_j(x)$ be the PSF associated with the kth subregion and let $i_j(x) = (h_j * o)(x)$ be the corresponding speckle image. To perform a bispectrum recovery from this information, form a bispectrum estimate $B_{I_k}(u,v)$ for each region. Then in the ensemble average, the phase of each region's bispectrum will match the object's bispectrum phase:

$$\arg \langle B_{I_k}(u,v) \rangle = \arg B_O(u,v). \tag{5}$$

Note that in general, each region will have a different diffraction cutoff, so for some k the phase on the left-hand side of Eqn. 5 could be undefined for some u and v.

A simple way of combining the bispectra of the subregions into a single bispectrum estimate is to calculate the sample variance of the estimates and use that to form a weighted mean bispectrum. Let $\sigma_k^2(u,v)$ be the sample variance of $B_{I_k}(u,v)$. Then let

$$B_{\text{syn}}(u,v) = \sum_k \frac{B_{I_k}(u,v)}{\sigma_k(u,v)} \Bigg/ \sum_k \frac{1}{\sigma_k(u,v)} \tag{6}$$

be the synthesized bispectrum estimate. Note that this is weighting by standard deviation, not by variance as one might expect. In simulation results, the standard deviation was found to produce a better result.

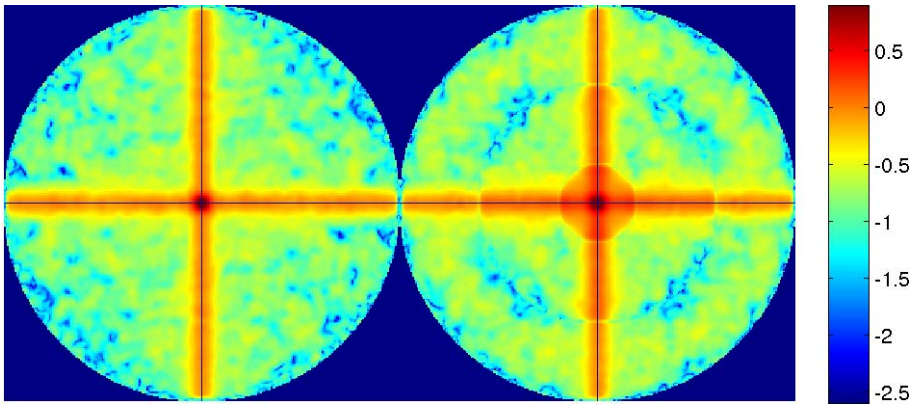

Full aperture Partitioned aperture

Figure 1. The logarithm (base 10) of the bispectrum SNR in the subplane $u = (x, 0)$, $v = (0, y)$. On the left, the bispectrum is formed from the full pupil. On the right, the bispectrum estimate is formed from an aperture divided into three concentric annuli. The C_n^2 profile was scaled to yield $D/r_0 = 16$.

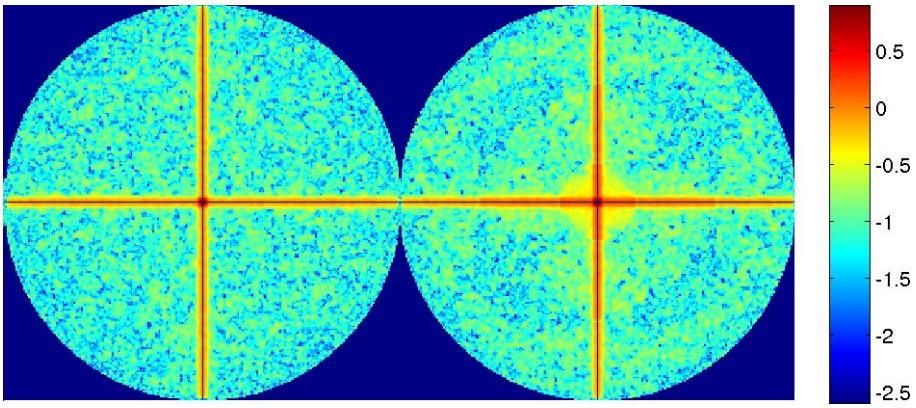

Full aperture Partitioned aperture

Figure 2. The bispectrum SNR for the full and partitioned aperture with $D/r_0 = 40$.

3. SIMULATION RESULTS

3.1 Simulation description

To test the performance of this technique, we simulated a system with a 3.6 m aperture collecting data at 30 Hz in the I band. The atmosphere is modeled using the Maui-3 C_n^2 profile, scaled to yield various turbulence strengths. The atmosphere is broken into four slabs to capture the effects of slew and wind. The FPAs are 256×256 CCDs with sky foreground and photon noise modeled, but no read noise. Unless otherwise noted, the results shown are for an aperture partitioned into three concentric annuli, a sidereal slew rate, a ground wind speed of 4 m/s, and one second's worth of data (30 frames).

3.2 SNR results

For conventional full-aperture speckle imaging, various authors [3–5] have derived analytic approximations of the SNR of the bispectrum estimate. These calculations are based on the assumption that the aperture contains a large number of statistically independent atmospheric cells, which is approximately true in the mid-frequency region with a full aperture. However, this does not hold for the annular subapertures that are of interest here. Instead, we depend on simulations to provide measurements of the bispectrum SNR.

Fig. 1 shows the bispectrum SNR in the plane $u = (x, 0)$, $v = (0, y)$ when $D/r_0 = 16$. The left side is obtained from the full aperture. The right side is the result obtained via Eqn. 6 from the partitioned aperture. On the left side, the usual features are visible [3]: very high SNR near the origin, high SNR along the $\|u\| \approx 0$ and $\|v\| \approx 0$ axes, and a plateau of

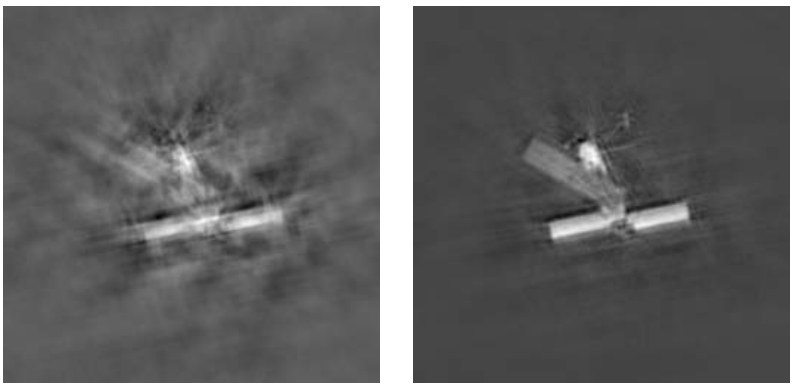

Full aperture Partitioned aperture

Figure 3. Reconstructed images from a full aperture (left) and partitioned aperture (right) with $D/r_0 = 64$ and sidereal slew rate. Both data sets were generated from the same simulated wavefronts. The target brightness was scaled to yield visual magnitude of 1, which gives a peak SNR of 820 on the full aperture FPA.

much lower SNR out to the diffraction limit. The partitioned aperture has a similar structure, but the regions of high SNR extend further out from the axes. A "ring" structure is visible in the SNR map due to the annular partitions of the pupil.

In Fig. 2, the turbulence strength has been increased to give $D/r_0 = 40$. The color scale matches that of Fig. 1, so the SNR is clearly lower everywhere. As before, the partitioned aperture yields higher SNR, especially in the region off-axis but close to the origin. The importance of this region to the quality of the object phase reconstruction is evident from Eqn. 2. If $B_O(u, v)$ is noisy when $\|u\| \neq 0$, $\|v\| \neq 0$, then the estimate of $O(u + v)$ obtained from $O(u)$ and $O(v)$ will also be noisy.

3.3 Image results

To get an idea of how the improved SNR translates into image quality, we now look at a series of comparisons between full-aperture and partitioned-aperture reconstructed images. In each case, the same wavefronts are used to generate the simulated images from which the reconstructions are formed.

Fig. 3 illustrates the case of $D/r_0 = 64$ for a bright (visual magnitude $m_v = 1$) target. Recall that partitioning the aperture both boosts the OTF and reduces the baseline redundancy noise. Boosting the OTF would result in less noise amplification in the higher spatial frequencies, but in this case the SNR is so high that there is virtually no sensor noise to amplify. On the other hand, there is a great deal of baseline redundancy noise, and by reducing it the partitioning method produces a much better result.

In Fig. 4, the target brightness is varied from 1st mag to 10th mag. In each case the partitioned aperture yields the superior result. This is somewhat counterintuitive, since splitting the aperture to form separate images means that each partitioned-aperture speckle image will have lower SNR than the full-aperture speckle images. However, under the conditions simulated here, this is not sufficient to outweigh the advantages of the partitioning technique. Presumably this would no longer be the case if the sensor read noise were sufficiently high.

As the turbulence strength increases (Fig. 5), the degree of baseline redundancy increases, causing the full-aperture images to suffer. Breaking up the pupil suppresses this source of error, greatly improving the reconstructed image quality.

Fig. 6 shows the effect of slew rate on image quality. As the slew rate increases, the phase in the pupil decorrelates more quickly. This improves the performance of the full-pupil results because redundancy noise can be effectively averaged out using independent realizations of the atmosphere. It has less effect on the partitioned-aperture setup, which enjoys a much lower level of redundancy noise.

Finally, we consider the effect of the changing the number of annuli into which the pupil is partitioned. As shown in Fig. 7, if there are too few annuli, then there is enough redundancy in each annulus to yield perceivable noise in the recovered image. However, as the number of annuli increases, the available light is split between more and more FPAs, reducing the SNR on each one. For the system modeled here, the best performance is obtained with 3 or 4 annuli.

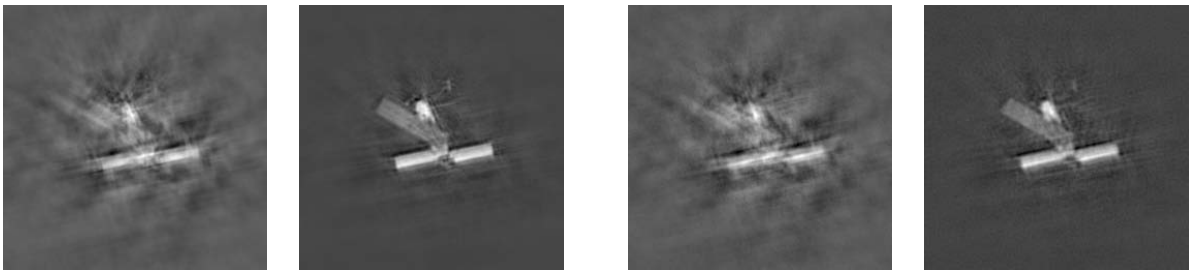

Full aperture Partitioned aperture Full aperture Partitioned aperture

$m_v = 1$ $m_v = 4$

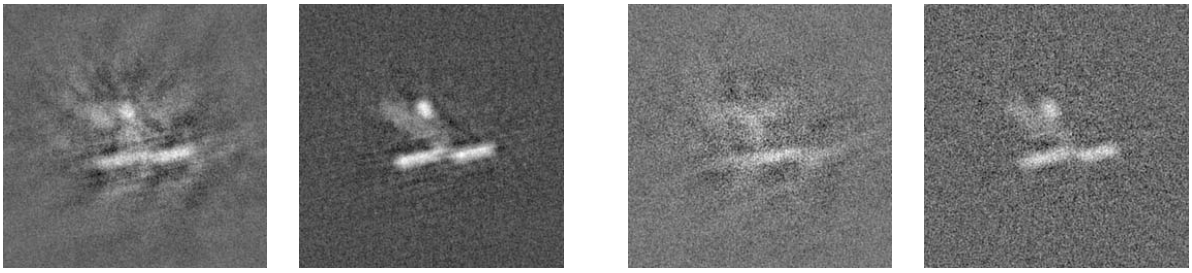

Full aperture Partitioned aperture Full aperture Partitioned aperture

$m_v = 8$ $m_v = 10$

Figure 4. Full aperture vs. partitioned aperture as a function of target brightness. The peak pixel SNR on the full aperture FPA varies from 13 at 10th mag to 820 at 1st mag.

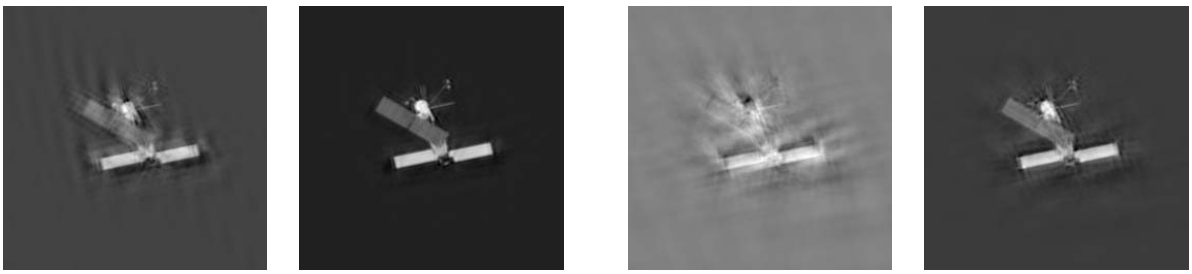

Full aperture Partitioned aperture Full aperture Partitioned aperture

$D/r_0 = 16$ $D/r_0 = 40$

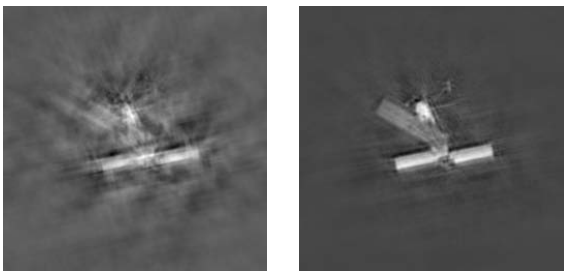

Full aperture Partitioned aperture

$D/r_0 = 64$

Figure 5. Full aperture vs. partitioned aperture as a function of turbulence strength. The increase in redundancy noise causes an obvious deterioration in the quality of the full-aperture results.

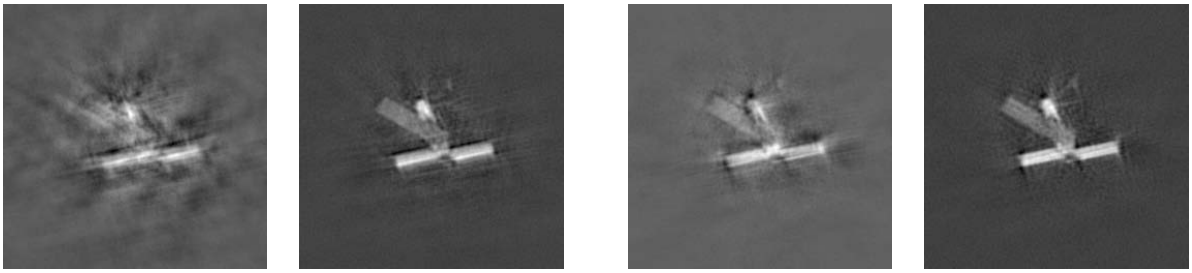

Full aperture Partitioned aperture Full aperture Partitioned aperture

Sidereal slew 0.02°/sec slew

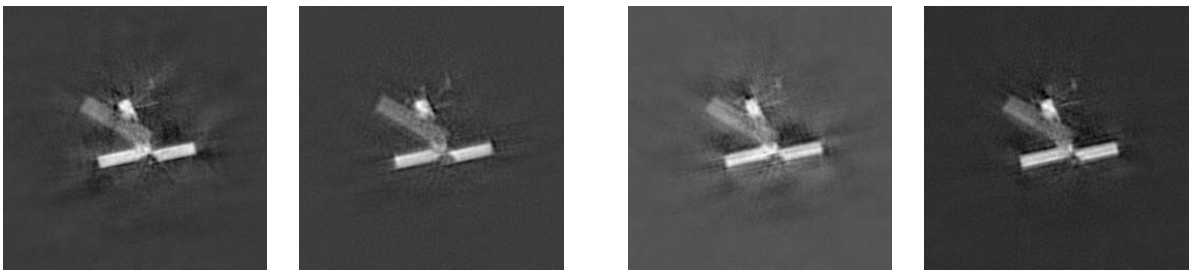

Full aperture Partitioned aperture Full aperture Partitioned aperture

0.2°/sec slew 0.5°/sec slew

Figure 6. Full aperture vs. partitioned aperture as a function of slew rate with $m_v = 4$. As slew rate increases, the measured atmospheric realizations become completely decorrelated, beating down redundancy noise.

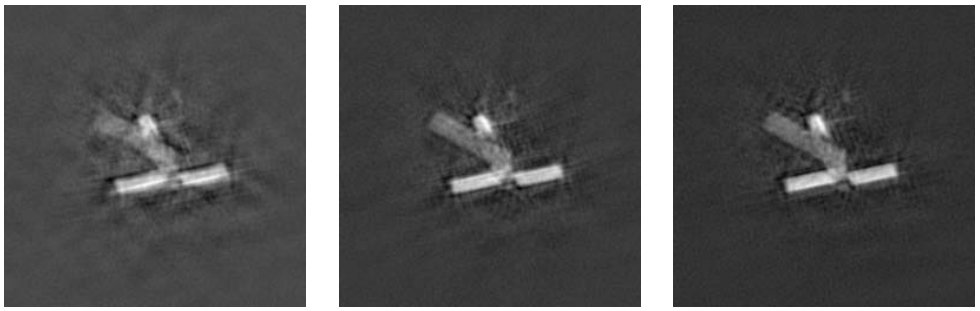

2 annuli 3 annuli 4 annuli

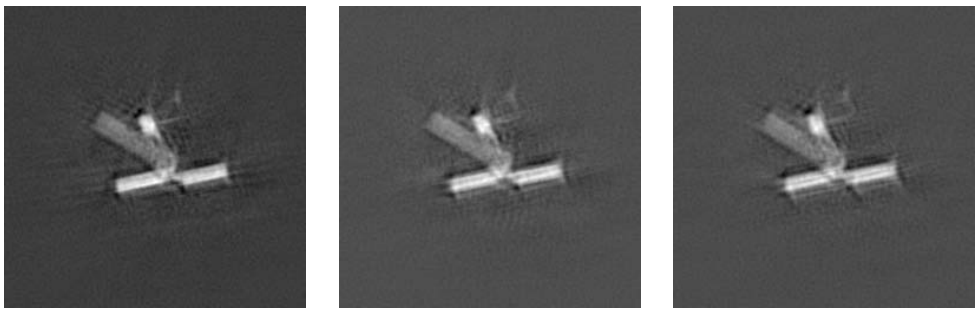

5 annuli 6 annuli 7 annuli

Figure 7. Partitioned-aperture results as a function of the number of annuli, with $D/r_0 = 64$ and $m_v = 4$. The trade-off between redundancy noise and signal level is apparent.

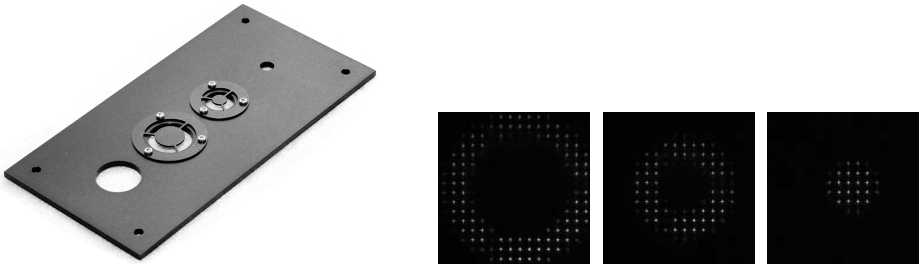

(a) (b)

Figure 8. Pupil masks. (a) Aperture mask plate installed in the sensor. (b) Shack-Hartmann images of each subaperture. Note that these were made with an internal source, so the secondary obscuration is not visible in the smallest mask.

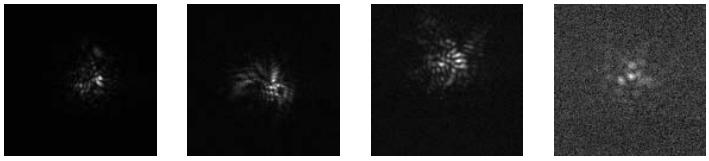

Full Outer Middle Inner

Figure 9. Data collected with each mask in place.

4. EXPERIMENTAL DESIGN

We conducted an experimental test of aperture partitioning using the GEMINI sensor on the MSSS 1.6 m telescope, which is capable of collecting critically-sampled imagery at over 200 Hz. To be operationally useful, a phase mask or mirror arrangement would be needed to partition the aperture so that all subapertures could be measured simultaneously. However, as an initial demonstration, we instead used a series of pupil masks to measure each subaperture in succession. This is a valid demonstration, since the bispectrum of each subaperture is estimated independently. However, it cannot be applied to fast-moving satellites, since the object pose changes noticeably in the time required to switch masks.

A set of four pupil masks were made in a steel plate (see Fig. 8a) and mounted on a motorized linear stage at a pupil in the system. Switching from one mask to another can be done from the sensor console and takes about two or three seconds. The masks include the full pupil and three annular subapertures. The outermost mask spans the entire 1.57 m pupil, the middle annulus has an outer diameter of 1.05 m, and the inner annulus is 0.53 m across. Within the inner annulus is the central obscuration of the telescope, which is 0.36 m across. Thus, the inner annulus has a thickness of about 8.5 cm and the middle and outer annuli are about 26 cm thick. Wavefront sensor images of each subaperture are shown in Fig. 8b.

In order to get a wide range of conditions, data was collected over two days (once in mid-morning and once in mid-afternoon) and three nights (all evening terminator). Stars and binary pairs were collected at elevation angles between 20 and 85 degrees. A variety of filters were used, typically in the 700-900 nm range. For each data set, seeing was estimated from the short-exposure imagery using the technique of von der Lühe [6]. Median daytime seeing was 3 cm and median nighttime seeing was 8 cm.

Fig. 9 shows data collected in each mask. It is easy to see the reduced resolution in the data from the middle and, especially, the inner subapertures due to the smaller pupil. Also, the data from the inner subaperture clearly has much lower SNR because the collection area for this mask is much smaller than for the others. This illustrates the point that although splitting the pupil into more subapertures would reduce redundancy noise, each one would also suffer more from sensor noise (read noise and shot noise) due to the reduced signal level.

5. EXPERIMENTAL RESULTS

To compare the relative performance of full-aperture and partitioned-aperture speckle imaging, we generated quasi-experimental extended-target data from the collected stars (although binary stars were collected, they were not analyzed for this study). This was accomplished by convolving each star frame (h) with a TASAT rendering of SEASAT (o), normalized

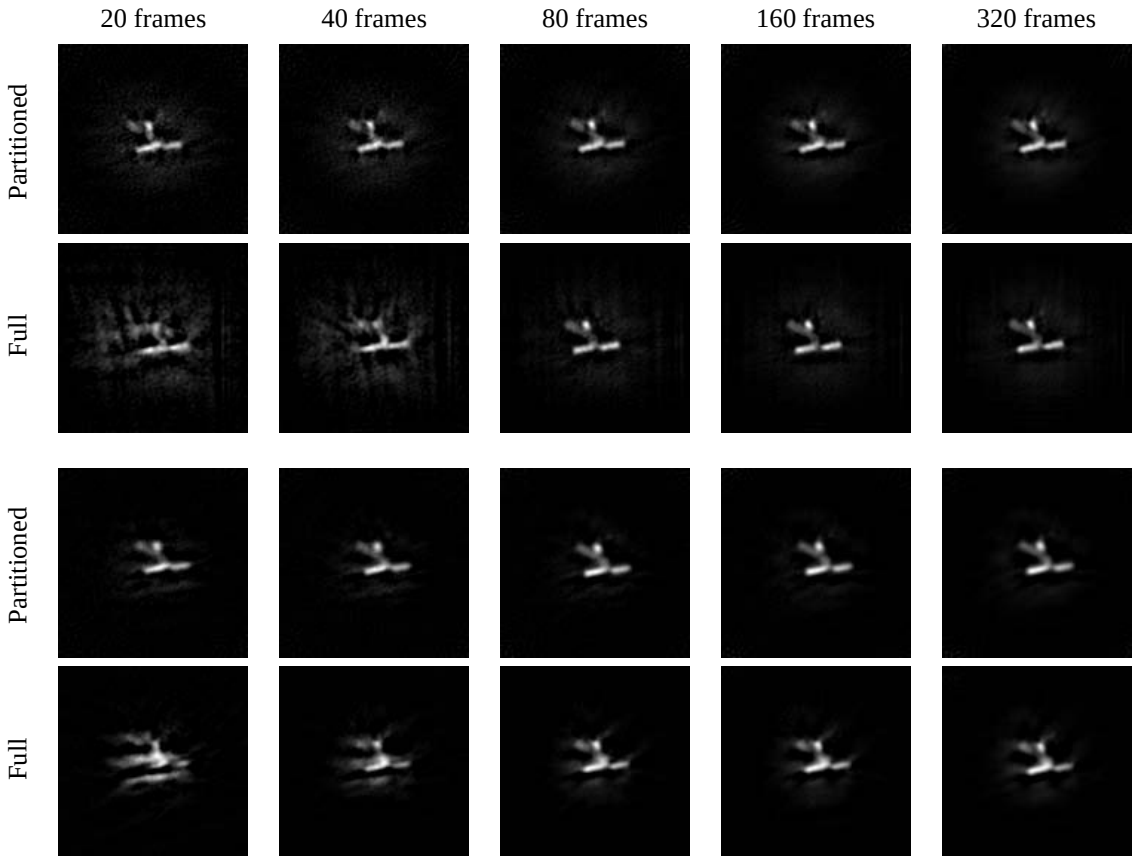

Figure 10. Reconstructions for two daytime data sets.

to $\sum o_i = 1$. One can see that this does not have valid photon statistics, so Gaussian noise with variance $(o - o^2) * h$ was added to each image to approximately corrects the statistics.

To form a reconstruction from the three-subaperture data, the bispectrum was estimated from the first N frames of each of the three masks. The object Fourier phase is recovered from the weighted average of the bispectra.

To form a reconstruction from the full-pupil data, three groups of $N/3$ consecutive frames were used. The groups were spaced several seconds apart. The purpose of this is to ensure that the partitioned-aperture method does not derive some advantage from the fact that the atmosphere has time to decorrelate while the pupil mask in the sensor is being changed.

Some example reconstructions are shown in Figs. 10 and 11. For most data sets, aperture partitioning produces a visually preferable result. In order to better quantify this, a second set of extended data was created using a resolution target as the pristine object. Then each reconstruction was visually assessed to determine the minimum resolvable feature size in pixels. The results of this procedure for each data set are plotted in Fig. 12.

Two trends are apparent in these results. First, severe seeing conditions (smaller r_0) consistently favor aperture partitioning. In particular, aperture partitioning produced a better result for all but one of the daylight data sets. This is consistent with the view that there is a tradeoff between redundancy noise and sensor noise. Using a partitioned aperture reduces redundancy noise, but by dividing the light between three separate focal planes, it experiences more sensor noise. As r_0 drops (as in the daytime, for example), redundancy noise becomes dominant. But in good seeing conditions, the lower sensor noise in the full-aperture data produces a better result.

Second, as more frames are processed together, the two methods tend to approach a common result. This is because as more frames are used, the average measured bispectrum approaches the true ensemble average even for the full-aperture case. In practice, the number of frames that can be processed together is dictated by the rate at which the object (the satellite) is changing pose.

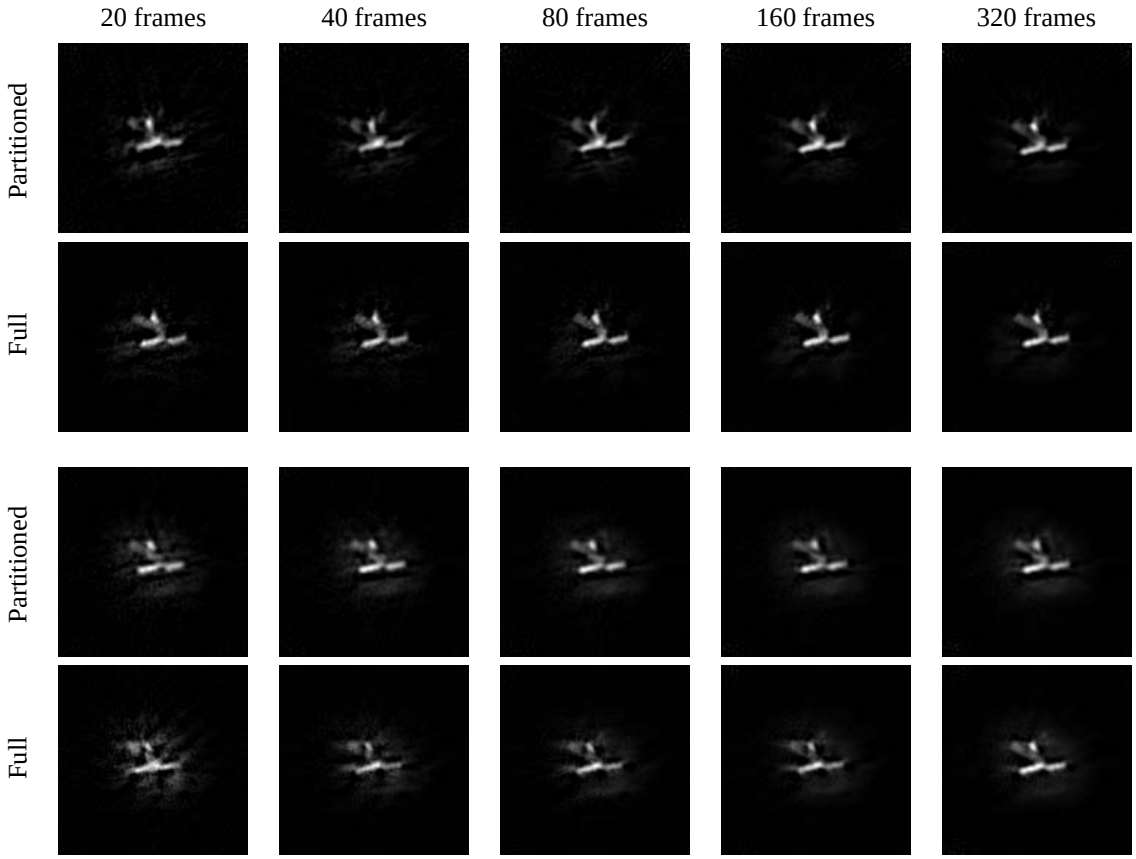

Figure 11. Reconstructions for two nighttime data sets.

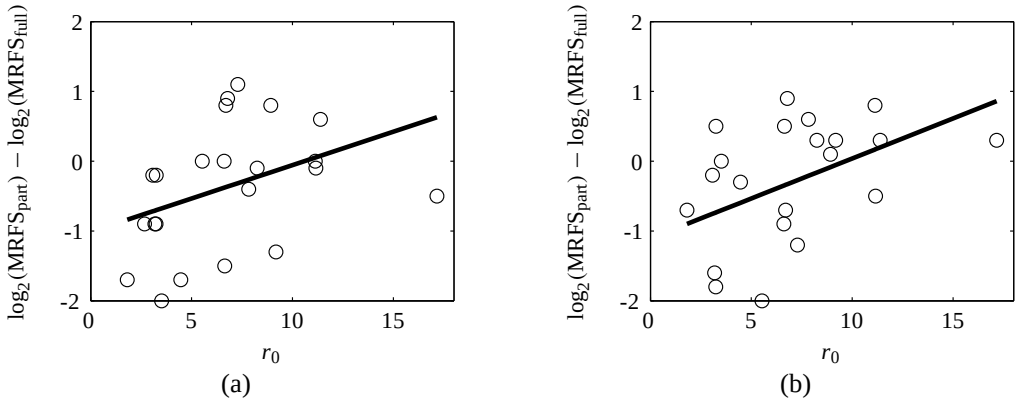

Figure 12. Difference in $\log_2$ of minimum resolvable feature size vs r_0 for (a) 20 frames and (b) 320 frames. Negative values indicate cases in which aperture partitioning produced the better result. Its advantage tends to diminish as r_0 increases.

6. CONCLUSIONS

We have described a technique for improving speckle imaging performance by partitioning the telescope aperture. In both simulations and experiments, we find that when $D/r_0 \gg 1$ and the slew rate is fairly low, it greatly outperforms conventional full-aperture imaging. Unlike aperture masking interferometry, this advantage is maintained even for dim targets.

ACKNOWLEDGMENTS

Invaluable engineering support was provided by Chris Shurilla, Ed Walker, and Chris Young. The author thanks Chuck Matson for his encouragement. This work was funded by the Air Force Office of Scientific Research through AFRL contract FA9451-05-C-0257.

REFERENCES

[1] Roggemann, M. C. and Welsh, B., *Imaging Through Turbulence*, CRC Press (1996).

[2] Haniff, C. A., Buscher, D. F., Christou, J. C., and Ridgway, S. T., "Synthetic aperture imaging at infrared wavelengths," *Monthly Notices of the Royal Astronomical Society* **241**, 51–56 (1989).

[3] Nakajima, T., "Signal-to-noise ratio of the bispectral analysis of speckle interferometry," *Journal of the Optical Society of America A* **5**(9), 1477–1491 (1988).

[4] Ayers, G. R., Northcott, M. J., and Dainty, J. C., "Knox-Thompson and triple-correlation imaging through atmospheric turbulence," *Journal of the Optical Society of America A* **5**(7), 963–985 (1988).

[5] Chelli, A., "The phase problem in optical interferometry: error analysis in the presence of photon noise," *Astronomy and Astrophysics* **225**, 277–290 (1989).

[6] von der Lühe, O., "Estimating Fried's parameter from a time series of an arbitrary resolved object imaged through atmospheric turbulence," *Journal of the Optical Society of America A* **1**(5), 510–518 (1984).

DISTRIBUTION LIST

DTIC/OCP
8725 John J. Kingman Rd, Suite 0944
Ft Belvoir, VA 22060-6218 1 cy

AFRL/RVIL
Kirtland AFB, NM 87117-5776 2 cy

Casey Pellizzari
Official Record Copy
AFRL/RDSM 1 cy